Progress in Physics of Applied Materials 6 (2026), Serial Number 12, 217-227

Semnan University

Progress in Physics of Applied Materials

journal homepage: https://ppam.semnan.ac.ir/

# Quantum Capacitance Enhancement of AlN Nanoribbon Via Transition Metal Doping: Density Functional Study

**Keyvan Moradian Koochaksaraei, Majid Vaezzadeh***

*Department of Solid-State Physics, Faculty of Physics, K. N. Toosi University of Technology, Tehran, Iran*

**ARTICLE INFO**

Article history:
Received: 7 October 2025
Revised: 25 December 2025
Accepted: 28 December 2025
Published online: 18 February 2026

Keywords:
Quantum Capacitance;
DFT;
AlN Nanoribbon;
Transition Metal Doping;
Surface Charge Density;
Anode;
Cathode Applications.

**ABSTRACT**

First-principles density-functional calculations are used to explore the influence of transition-metal dopants (Sc, Ti, V, Mn, Fe, Co) on the electronic structure, stability and quantum capacitance (QC) of zig-zag AlN nanoribbons. Substitutional doping at either the edge or center of the ribbon is found to introduce mid-gap states that markedly increase the density of states near the Fermi level, yielding up to a 40-fold enhancement in QC related to the pristine lattice. Vanadium-doped configurations possess the highest cohesive energy (−5.85 eV per atom) and the largest surface-charge density (40 μC $cm^{-2}$ at +0.6 V vs −0.6 V), identifying them as optimal anode materials. Conversely, cobalt-rich ribbons deliver superior cathodic capacity, whereas Mn-doped systems exhibit almost symmetric charge storage. Phonon spectra confirm dynamic stability for all considered dopants. The results provide quantitative design rules for tailoring of AlN nanoribbons as high-rate, high-capacity electrodes in advanced supercapacitors.

## 1. Introduction

The excessive use of fossil fuels by modern societies is recognized as the primary driver of global warming, highlighting the urgent need to transition to renewable and clean energy sources such as solar, hydro, and wind power. These renewable resources, because of their strong potential to reduce environmental harm, have become indispensable choices for environmental preservation. However, the success of a sustainable energy supply from these sources is highly dependent on the development of efficient energy storage systems. Among various solutions, rechargeable batteries and electrochemical supercapacitors have gained considerable attention as key technologies for energy storage [1,2].

Supercapacitors, as advanced energy storage devices, have gained prominence in modern technologies due to their high-power density, rapid charge-discharge rates, and long cycle life [3]. However, their relatively low energy density compared to other storage technologies, such as batteries, remains a fundamental limitation. The performance of supercapacitors is strongly influenced by the materials used for their electrodes. These materials must possess specific characteristics, including high electrical conductivity, a large surface area, chemical and thermal stability, and high specific capacitance. These properties directly affect the quantum capacitance (QC) of the material, which in turn determines its ability to store charge and energy [4]. Quantum capacitance is dependent on the material's electronic structure, including its energy gap and density of states (DOS), making it a key parameter

* Corresponding author.
*E-mail address:* Majid@kntu.ac.ir

**Cite this article as:**

Moradian Koochaksaraei, K. and Vaezzadeh, M., 2026. Quantum capacitance enhancement of AlN nanoribbon via transition metal doping: Density Functional Study, *6*(3), pp.217-227. DOI: 10.22075/ppam.2025.39297.1176

in optimizing supercapacitor performance. Nevertheless, the relatively low energy density of supercapacitors compared to other energy storage technologies, such as batteries, remains a significant challenge [5, 6].

This limitation stems from the structural characteristics of electrode materials and the intrinsic nature of energy storage processes in supercapacitors. To address this challenge, several strategies have been proposed, including: (i) nanostructuring conventional electrode materials to enhance specific capacitance, (ii) developing novel electrode materials with higher specific capacitance, (iii) utilizing ionic or organic electrolytes with wide voltage windows, and (iv) designing asymmetric supercapacitors using different materials across various voltage ranges. Among these approaches, one-dimensional (1D) nanomaterials have emerged as promising candidates for supercapacitor electrodes due to their unique properties. These materials exhibit high electrical conductivity, extensive surface area, suitable chemical and thermal stability, and significant specific capacitance. Furthermore, a key advantage of 1D nanomaterials is their tunable atomic and electronic structures, which directly affects their quantum capacitance.

Quantum capacitance, which refers to the ability of materials to store charge at the electrode surfaces on a nanometric scale, is enhanced in 1D nanomaterials due to their dimensional constraints, thus contributing to improved supercapacitor performance [7]. Recent research in applied physics and materials science, as exemplified by studies published in this journal, continues to explore the intricate structure-property relationships in advanced nanostructured materials, including complex oxides [8], nanocomposites [9], and functional nanoparticles [10]. Our work contributes to this ongoing effort by applying first-principles calculations to unravel the quantum capacitive behavior of a distinct class of low-dimensional nitrides. Examples include graphene nanoribbons (GNRs) [11], transition metal dichalcogenides (TMDs) such as $MoS_2$ [12], $WSe_2$ [13], and MXenes [14]. By improving quantum capacitance, these materials significantly contribute to enhancing the energy density of supercapacitors.

Numerous studies have investigated the quantum capacitance of graphene nanoribbons (GNRs). Kliros [11], for instance, examined the effect of uniaxial strain on the quantum capacitance of GNR-based devices. Using an analytical model, this research calculated the carrier density and quantum capacitance of these nanoribbons, showing that uniaxial tension induces significant changes in the bandgap and effective mass, which directly affect the quantum capacitance. In another study, the quantum capacitance of hybrid graphene-copper nanoribbons was explored, revealing that nanoribbons with widths below 3 nanometers significantly enhance quantum capacitance, making these structures highly suitable for energy storage applications. Additionally, a separate investigation examined three different configurations of armchair graphene nanoribbons (AGNRs): H-AGNR-H, Cu-AGNR-H, and Cu-AGNR-Cu. This research evaluated parameters such as structural stability, dynamic stability, quantum capacitance, and surface charge to assess the performance of these nanoribbons as potential materials for supercapacitors. Experimental evidence has also demonstrated the feasibility of synthesizing group III nitride nanoribbons, such as aluminum nitride (AlNNRs) and gallium nitride (GaNNRs) [15].

This breakthrough has opened a new avenue for the development of novel materials. The present study, using density functional theory (DFT) calculations, investigates the impact of manganese doping at different positions, ranging from the center to the edge, of AlN nanoribbons on their electronic behavior and quantum capacitance. The results show that the position of the impurity atom significantly influences spin polarization, the density of electronic states near the Fermi level, and surface charge density. Specifically, variations in the location of the manganese atom lead to substantial changes in the electronic properties of the nanoribbons, including energy configurations and surface charge distribution. These findings suggest that by carefully controlling the placement of dopants, the electronic properties and quantum capacitance of the nanoribbons can be optimized, thereby enhancing their performance in energy storage applications. This study not only expands our understanding of the role of doping in nanomaterials, but also contributes to the design and optimization of materials for advanced electronic devices and energy storage technologies.

## 2. Computational Details

All DFT calculations were performed using the QUANTUM ESPRESSO package [16] with the Perdew–Burke–Ernzerhof (PBE) generalized gradient approximation (GGA) functional [17]. The PBE-GGA functional was chosen because of its computational efficiency and established accuracy in capturing electronic and magnetic trends in 3d transition metal-doped low-dimensional systems [18]. While more advanced functionals (e.g., hybrid or DFT+U) could provide a more accurate description of localized d-states, PBE functional is widely adopted in comparable studies and suffices for capturing relative trends in quantum capacitance and charge storage, which is the primary focus of this work. A kinetic energy cutoff of 820 eV was used for the plane-wave expansion. The Brillouin zone was sampled using a 24×1×1 Monkhorst–Pack k-point grid. A vacuum spacing of 25 Å was applied in non-periodic directions to prevent inter-ribbon interactions. These parameters were selected based on convergence tests, ensuring that total energy changes were less than 1 meV/atom upon further refinement of the k-point grid or vacuum size. Energy and force convergence thresholds were set to $10^{-10}$ eV and 0.0001 eV/Å, respectively. Spin-polarized calculations were performed for all doped systems reflecting the magnetic nature of transition metal dopants. All simulations were conducted at room temperature (T = 300 K), which is explicitly included in the Fermi-Dirac distribution used for quantum capacitance evaluation.

The doping concentration was approximately 4.5% per 22-atom unit cell. Dopant atoms replaced aluminium atoms at three non-equivalent sites: A (upper zigzag edge), B

(geometric center), and C (lower zigzag edge). The transition metals Sc, Ti, V, Mn, Fe, and Co were selected to systematically cover a range of d-electron occupations ($d^1$ to $d^7$) and magnetic behaviors. While Cr ($d^5$) and Ni ($d^8$) are also important members of the 3d series, their exclusion was intended to enable a focused investigation while still capturing the essential trends across the series, particularly the transition from non-magnetic (Sc, Ti) to strongly magnetic (V, Mn, Fe) dopants and the effect of near-filled d-shells (Co). Phonon spectra were computed to confirm dynamical stability. Formation energies and magnetic moments were also evaluated.

To assess the dynamical stability of pristine and doped AlN nanoribbons, we calculated their phonon spectra. Figure 1 shows the phonon dispersion for pristine and V-doped AlN nanoribbons. The absence of imaginary frequencies confirms that all structures are dynamically stable. Similar results were obtained for other dopants. Cohesive and formation energies further support the thermodynamic stability of the doped systems, with vanadium demonstrating the greatest stability among all positions.

## 3. Results and Discussion

Aluminum nitride (AlN) is a two-dimensional material with a hexagonal crystal structure, where aluminum and nitrogen atoms are arranged flat and orderly within a single plane. The lattice parameter of this structure is a=b=3.12 Å [19-21]. In this study, AlN nanoribbons with zigzag edges were extracted from this structure and analyzed to investigate their energy storage capacity. The AlN nanoribbon, with its large and direct bandgap, has both valence and conduction band edges located at the Γ point. For this study, a nanoribbon with a cross-chain structure consisting of 22 atoms and a width of 32 Å (3.2 nm) was selected. Figure 1 shows the crystal structure and band structure of this nanoribbon. Analysis revealed a GGA bandgap of 3.0 eV [22], and the lattice parameter was calculated as $a_{ribbon}$= 5.39 Å along periodic direction. Due to its significant bandgap, this material is unsuitable for electrical conduction and electron exchange applications, such as charge storage and use as an electrode.

In this study, transition metals were positioned at three different non-equivalent sites within the nanoribbon structure, with these positions depicted in Figure 2. In position A, the transition metal atom is located near the upper edge of the nanoribbon. In position B, the metal atom is placed at the geometric center of the nanoribbon, while in position C, the metal atom is situated along the lower edge. Six different transition metals, namely Sc, Ti, V, Mn, Fe, and Co, were considered for each position as dopant. The initial structures of the AlN nanoribbon doped with transition metals were optimized to achieve structural equilibrium. The considered configurations, schematically illustrated in Figure 2, identify the most stable structures for each specific position. The primary objective of this research is to analyze the quantum capacitance of the AlN nanoribbon doped with transition metals and to investigate the impact of changes in the density of states on this property. Variations in the DOS, influenced by the different positions of the metal atoms, are expected to affect the quantum capacitance of the nanoribbon.

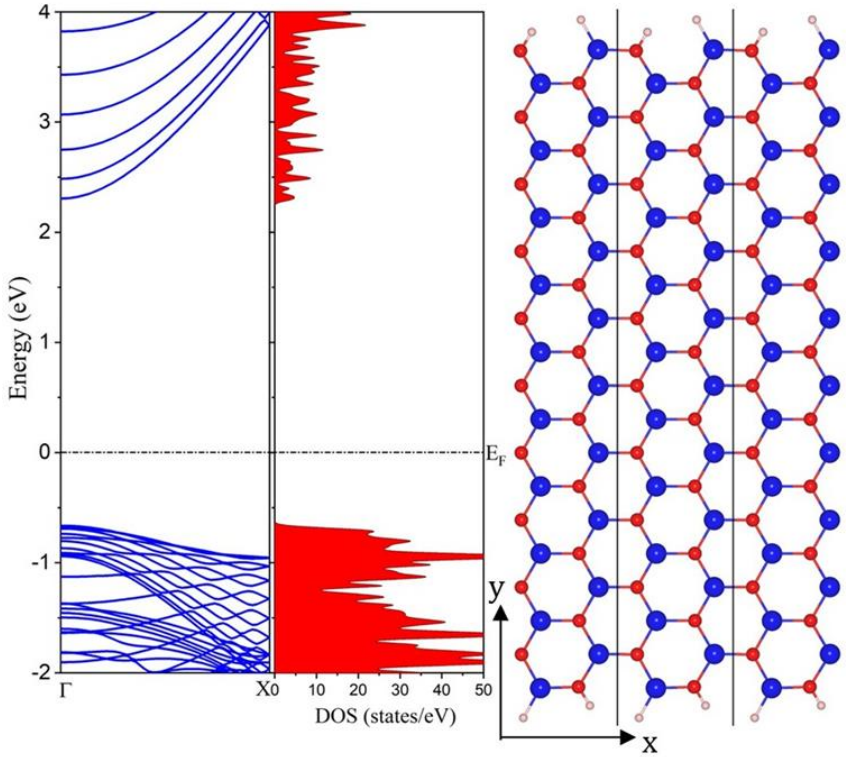


**Fig. 1.** Atomic structure and band structure of pristine zigzag AlN nanoribbon (22 atoms, 3.2 nm width). The bandgap is approximately 3 eV (GGA-PBE).

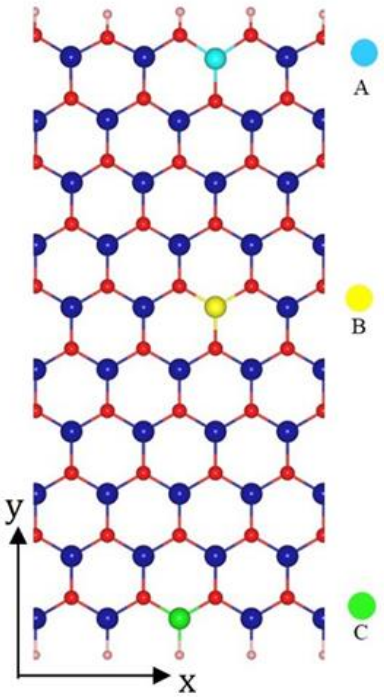


**Fig. 2.** Optimized structures of TM-doped AlN nanoribbons at the upper edge (A), center (B), and lower edge (C) sites.

The subsequent discussion will focus on the investigation of electrochemical charge storage mechanisms in nanomaterials through the calculation of their quantum capacitance. Quantum capacitance, denoted as $C_q$, and defined as $C_q=dq/d\phi$, is a crucial characteristic in assessing the energy storage performance of materials. It is directly related to the density of electronic states (DOS) near the Fermi level and can be calculated using the following relation [23-25]:

$$C_q(T) = e^2 \int_{-\infty}^{+\infty} D(E) \left( -\frac{\partial f(E,\mu,T)}{\partial E} \right) dE \quad (1)$$

where *f(E,μ,T)* is the Fermi–Dirac distribution, μ represents the chemical potential, which corresponds to the energy level at which the probability of electron occupation is 50% and shifts with the applied potential, $k_B$ is the Boltzmann constant, and D(E) is the density of states.

$$-\frac{\partial f(E,\mu,T)}{\partial E} = \frac{1}{4k_BT} sech^2 \left( \frac{E-\mu}{2K_BT} \right) \quad (2)$$

The surface charge (σ) at a specific local potential is calculated through the following integral, taking into account the system's characteristics and the electronic distribution at the corresponding potential:

$$\sigma = \int_0^{\Phi} C_q \, d\Phi \quad (3)$$

In this equation, $C_q$ represents the quantum capacitance, which depends on the local potential and the system's characteristics, and ϕ denotes the potential that changes from zero to a specific value ϕ. This integral precisely calculates the surface charge, taking into account the distribution of quantum capacitance across different potential regions. The investigation of quantum capacitance reveals that the AlN nanoribbon exhibits a zero $C_q$ value due to the absence of electronic states around the Fermi level. This issue can be improved by employing methods such as doping or structural modifications, which can increase the density of states near the Fermi level, thereby enhancing the quantum capacitance of the system.

In this research, the effect of doping with Sc, Ti, V, Mn, Fe, and Co atoms at three different structural positions, namely positions A, B, and C of the AlN nanoribbon, has been investigated. Due to the specific nature of the d-orbitals in transition metal elements and their ability to generate significant magnetic moments, all electronic calculations have been performed considering spin polarization. Figure 3 displays the electronic DOS distribution for 18 different configurations resulting from these doped systems.

The results of the electronic density of states calculations indicate that the various dopants exhibit different electronic characteristics. For the Sc-doped configuration, due to the small number of electrons in the d-orbitals, no magnetic moment is generated, and no significant changes are observed in the density of states near the Fermi level. Titanium exhibits a similar behavior; however, its effect is slightly more pronounced compared to scandium. Titanium induces slight changes in the DOS peaks and creates additional states around the Fermi level for all three positions. Nevertheless, the magnetic moment generated by this atom is also relatively small.

Vanadium, due to the partially filled nature of its d-orbitals, generates a stronger magnetic moment compared to the previous two elements. This atom enhances the interaction between its d-orbitals and the p-orbitals of nitrogen atoms, creating broad peaks in the density of states near the Fermi level. In this configuration, a metallic behavior is clearly evident, with three significant effects observed simultaneously: changes in the distribution of the density of states, the creation of additional states around the Fermi level, and the generation of a stronger magnetic moment compared to the two previous cases across all positions.

For the manganese atom, additional states in the density of states near the Fermi level have been created at all three positions, and a magnetic moment has also been induced. In this configuration, the highest density of states near the Fermi level is observed at the center position. For the iron atom, compared to manganese, the distribution of the density of states has changed, with the peaks of the density of states around the Fermi level spreading, particularly at B and C positions. For the cobalt atom, additional states are formed, with the highest number of states around the Fermi level observed at position B.

Doping causes a disruption in the symmetry of the orbitals, leading to changes in the orbital contributions around the Fermi level compared to the pure state. For the vanadium atom, the density of states around the Fermi level is significantly enhanced compared to other states. The results indicate that the doped atoms of Ti, Mn, Fe, and Co do not show significant amounts of density of states around the Fermi level, but the symmetry breaking of the bond leads to an increased charge accumulation in the energy range of -1 to +1 eV around the Fermi level. For easier comparison, the DOS plots for all configurations have been adjusted to similar ranges for both the x and y axes. This increase is primarily observed in the valence band states within the energy range of -1 to 0 eV.

For a more detailed understanding of orbital contributions, projected density of states (PDOS) analysis was performed for all doped configurations (not shown). The PDOS confirms that the newly introduced states near the Fermi level predominantly arise from the d-orbitals of the transition metal dopants, with varying degrees of hybridization with the p-orbitals of neighboring nitrogen atoms. In particular, vanadium exhibits strong d-p hybridization, leading to broad and intense peaks near EF, consistent with its metallic behavior and highest quantum capacitance. In contrast, the PDOS for Sc and Ti shows minimal d-orbital contribution near EF, explaining their limited impact on Cq. This orbital-resolved analysis directly links the electronic configuration of the dopant, the resulting hybridization, and the enhancement in quantum capacitance.

To quantify this enhancement, we evaluate the integrated density of states within ±0.5 eV of the Fermi level ($N_{Ef}$). The value of $N_{Ef}$ rises from nearly 0.0 states/eV in the pristine AlN nanoribbon to approximately 2.6–3.2 states/eV for the vanadium-doped system at position B, and to about 0.6–1.1 states/eV for the manganese-doped system at position B. This marked increase in the number of accessible electronic states near the Fermi level provides a direct electronic-structure explanation for the observed boost in quantum capacitance.

In general, the impact of impurities on the electronic properties depends on the energy difference between the orbitals of the host structure, i.e., the AlN nanoribbon, and the impurity atoms (Sc, Ti, V, Mn, Fe, Co). This energy difference can lead to changes in the system's electronic characteristics, including shifts in the Fermi level, electron density, and ultimately the electronic properties of the system. The presence of more or fewer impurity electrons causes the Fermi level to shift toward either the valence band or the conduction band. Additionally, structural rearrangement induced by the doping process leads to changes in the orbital arrangements of the bonds, which can result in the splitting of the DOS or the creation of localized impurity states near the Fermi level. These effects lead to significant charge accumulation around the Fermi level, which is crucial for quantum capacity and energy storage.

To demonstrate the stability of the systems, the cohesive energy was calculated. The cohesive energy of the doped structures, shown in Figure 2, was calculated using the following formula [21]:

$$E_{coh} = \frac{E_{X-AlN} - E_x - mE_{Al} - mE_N}{m+n+1} \quad (4)$$

Where $E_{x\text{-}AlN}$, $E_x$, $E_{Al}$ and $E_N$ represent the total energy of the doped system and isolated impurity atoms, Al and N atoms, respectively. The indices n and m denote the total number of Al and N atoms in the doped AlN nanoribbon. The calculated cohesive energies for the systems are summarized in Table 1.

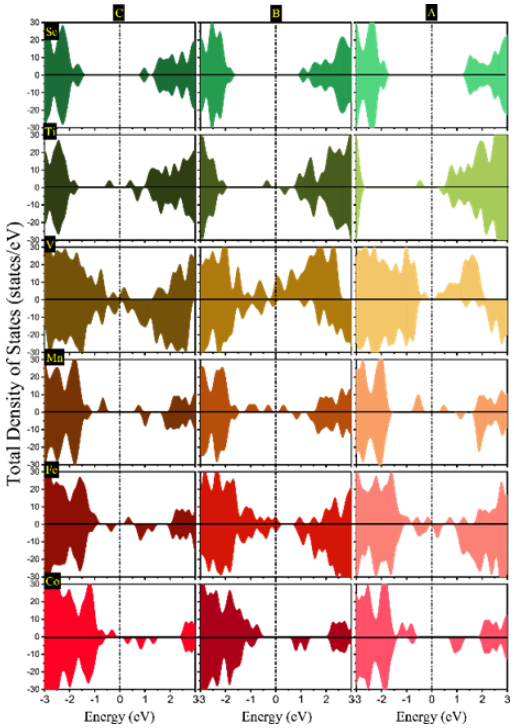


**Fig. 3.** Total DOS of TM-doped AlN nanoribbons. Vanadium shows strongest enhancement near the Fermi level.

**Table 1.** Calculated binding energies (in eV per atom) for doped structures at positions A, B, and C.

| | Sc | Ti | V | Mn | Fe | Co |
|---|---|---|---|---|---|---|
| A | -3.307 | -2.755 | -5.852 | -4.421 | -3.848 | -3.356 |
| B | -3.307 | -2.753 | -5.613 | -4.420 | -3.363 | -3.710 |
| C | -3.748 | -3.134 | -5.094 | -4.413 | -3.351 | -3.410 |

The nearly identical cohesive energies for Sc at the edge (A) and near-center (B) positions (-3.307 eV) suggest a weak dependence of its bonding on the local coordination, which can be attributed to its low d-orbital occupancy ($d^1$) and resulting delocalized bonding character.

The results indicate that all six transition metal atoms exhibit appropriate structural stability, with their cohesive energies ranging from -3 to -6 eV per cell. Moreover, cohesive energies showed minimal variation across doping sites (A, B, and C) for all impurity atoms. A comparison of the results reveals that doping with vanadium atoms provides greater stability compared to other transition metals, followed by doping with manganese, iron, and cobalt atoms in order of preference.

Using Equations 2 and 3 and calculating the total density of states (Fig. 3), the quantum capacitance ($C_q$) and surface charge storage (σ) for the doped AlN nanoribbons were evaluated and are presented in Figure 4. The results illustrated that doping with transition metals leads to significant improvements in these parameters. This enhancement is clearly attributed to the increased density of states near the Fermi level, which is induced by the presence of transition metal dopants. These impurity atoms alter the orbital contributions of the AlN nanoribbon and cause a rearrangement of orbital energies. These changes result in an increase in the number of accessible electronic states near the Fermi level, ultimately enabling the nanoribbon to exhibit greater charge storage capability and improved quantum capacitance. Therefore, the presence of impurity atoms in the nanoribbon structure plays a crucial role in enhancing its electronic performance.

As shown in Figure 4 for the system doped with vanadium atom, doping with transition metal atoms generally results in an increase in quantum capacitance and surface charge storage across the entire range of applied voltages compared to the pristine AlN nanoribbon. This improvement is also evident for systems doped with manganese, iron, and cobalt atoms. These atoms, due to the unique characteristics of their d-orbitals, form stronger interactions with nitrogen and aluminum atoms. When these transition metals are introduced into the nanoribbon, electronic rearrangements occur, leading to an increase in unoccupied states above the Fermi level, which are primarily associated with the d-orbitals of the transition metal atoms. As a result, the quantum capacitance of systems doped with these atoms improves significantly at positive voltages (see Fig. 4).

To evaluate the performance of materials as cathode or anode electrodes, the surface charge density (σ) and the electrode surface area (S) were analyzed in the voltage range of -0.6 to +0.6 V for various doped AlN configurations. σ quantifies the amount of electric charge per unit area on a material's surface, critical for analyzing electrode behavior. The results for σ are presented in Figure 5.

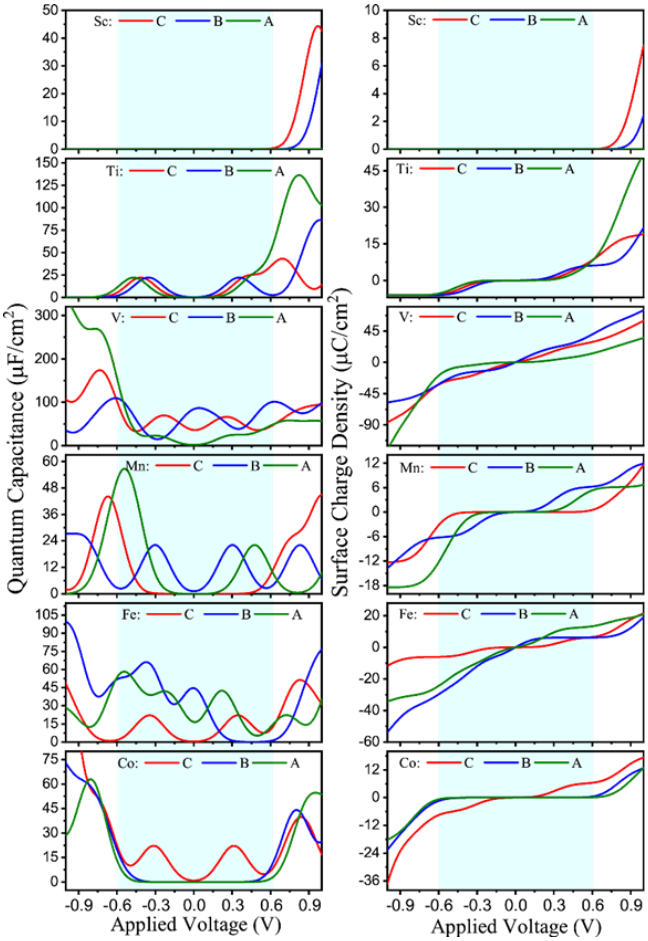


**Fig. 4.** Quantum capacitance (Cq) vs. potential for TM-doped AlN nanoribbons.

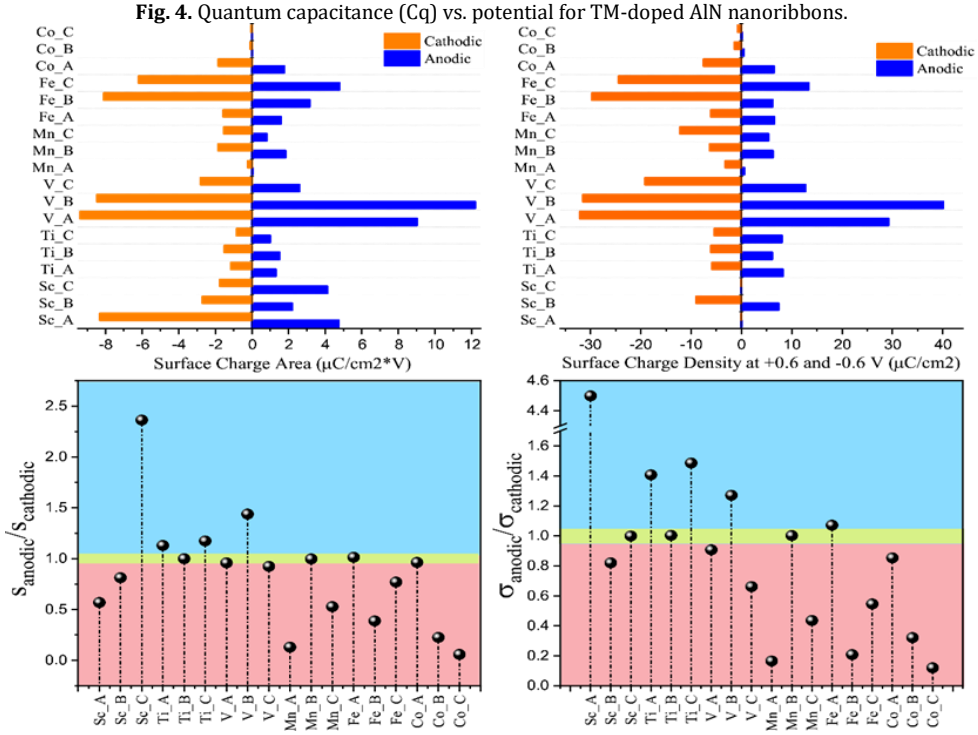


**Fig. 5.** Surface charge density (σ) and total surface charge (S) as a function of applied voltage for various doped AlN configurations.

The results presented in Figure 5 were compared with established criteria from previous studies for identifying suitable electrode applications [22].

$$Anode: \frac{\sigma_{anodic}}{\sigma_{cathodic}} > 1.05, Cathode: \frac{\sigma_{anodic}}{\sigma_{cathodic}} > 0.95, Symmetric: 0.95 < \frac{\sigma_{anodic}}{\sigma_{cathodic}} < 1.05 \quad (5)$$

Additionally, an alternative approach was introduced, involving the integrating the surface charge density over the applied voltage range to provide a more comprehensive evaluation of electrode performance. The charge density was analyzed within two voltage ranges: 0 to +0.6 V and -0.6 to 0 V. The results of both methods are presented in Figure 7. Accordingly, the considered criteria are as follows [22]:

$$Anode: \frac{S_{anodic}}{S_{cathodic}} > 1.05, \quad Cathode: \frac{S_{anodic}}{S_{cathodic}} > 0.95, \; Symmetric: 0.95 < \frac{S_{anodic}}{S_{cathodic}} < 1.05 \tag{6}$$

Where and S represent the surface charge density and the integral of the surface charge density, respectively. It is important to note that the electrode assignments (anode/cathode) based on the quantum capacitance asymmetry are made within the limited voltage window of –0.6 to +0.6 V, which is typical for aqueous electrolytes. In a real supercapacitor device, the operational voltage window is determined by the electrochemical stability of the electrolyte. The predicted behavior suggests that V-doped AlN nanoribbons are more favorable for positive charge storage, functioning effectively as anodes in a symmetric or asymmetric configuration with a suitable cathode material. Furthermore, the total capacitance of an electrode in practice is a series combination of the quantum capacitance (QC) studied here and the double-layer capacitance (Cdl). While this work focuses on enhancing QC, a high Cdl (e.g., from a large accessible surface area) is also essential for achieving high total capacitance. Future studies should consider the combined contribution of QC and Cdl for a complete assessment.

The results show that vanadium doping has the lowest formation energy (around 0.4–0.6 eV) among all considered dopants, indicating it is the most thermodynamically favorable to incorporate into the AlN lattice. This finding aligns perfectly with its highest cohesive energy (Table 1) and confirms V as the optimal dopant from a stability perspective. In contrast, Co and Fe exhibit higher formation energies (>1.2 eV), suggesting their incorporation would be less favorable under equilibrium growth conditions. The relatively low formation energies for all dopants (especially V, Ti, Mn) support the experimental viability of synthesizing such doped nanoribbons. The electrode classification based on both σ and S criteria is summarized in Figure 6. As shown, vanadium-doped systems exhibit strong anodic behavior, cobalt-doped systems act as cathodes, while manganese-doped systems display nearly symmetric charge storage.

In addition to electronic properties, the vibrational behavior of pristine and doped nanoribbons was analyzed through phonon dispersion curves, as shown in Figure 7.

The phonon dispersion curves of pristine AlN along the Γ–X direction are presented in Figure 6. The absence of imaginary frequencies confirms the dynamical stability of the pristine lattice. The acoustic branches exhibit the expected linear behavior near the Γ point, while the optic branches are well separated at higher frequencies, consistent with previous reports.

Our findings revealed that both methods provided similar results for identifying the electrodes. Specifically, vanadium-doped systems were predicted to function as anode electrodes, while cobalt-doped systems were identified as cathode electrodes. For manganese-doped systems, the $\sigma_{anodic}/\sigma_{cathodic}$ method indicated a stronger tendency towards anodic behavior, whereas the $S_{anodic}/S_{cathodic}$ method predicted a more symmetrical behavior. The numerical values corresponding to these calculations are presented in Table 2.

The quantum capacitance (QC) and surface charge density (σ) were calculated using Equations (1)–(3). As shown in Figure 4, doping with transition metals significantly enhances QC compared to the pristine nanoribbon. Among the doped systems, vanadium ones exhibit the highest quantum capacitance, particularly at position B, due to strong hybridization and high DOS near the Fermi level. Surface charge analysis (Fig. 5) reveals that V-doped configurations are ideal for anode applications, while Co-doped systems are better suited as cathodes. The calculated total surface charge (S) further supports these assignments (Table 2).

The introduction of transition metal dopants also significantly alters the magnetic properties of the nanoribbons. As summarized in Table 3, elements such as vanadium (V), manganese (Mn), and iron (Fe), with their partially filled d-orbitals, exhibit significant magnetic moments. This magnetic behavior is closely linked to the emergence of new electronic states near the Fermi level and influences the spin-polarized charge storage mechanism. In contrast, scandium (Sc) and titanium (Ti) exhibit negligible magnetic moments due to their electronic configurations.

To further evaluate the thermodynamic feasibility of incorporating transition metal dopants into the AlN nanoribbon, we calculated the defect formation energy ($E_f$) for each substitutional dopant at the three sites (A, B, C) using the following equation:

$$E_f[TMAl] = E_{tot}[AlN:TM] - E_{tot}[AlN\ pristine] - \mu_{TM} + \mu_{Al} \tag{7}$$

Here, $E_{tot}[AlN:TM]$ and $E_{tot}[AlN\ pristine]$ are the total energies of the doped and pristine systems, respectively, obtained from our DFT calculations. The chemical potential of the dopant atom ($\mu_{TM}$) is taken as the energy per atom in its bulk metallic phase (e.g., body-centered cubic for V, face-centered cubic for Co), and $\mu_{Al}$ is referenced to the energy per atom in bulk Al (face-centered cubic). The calculated $E_f$ values are summarized in Table 4.

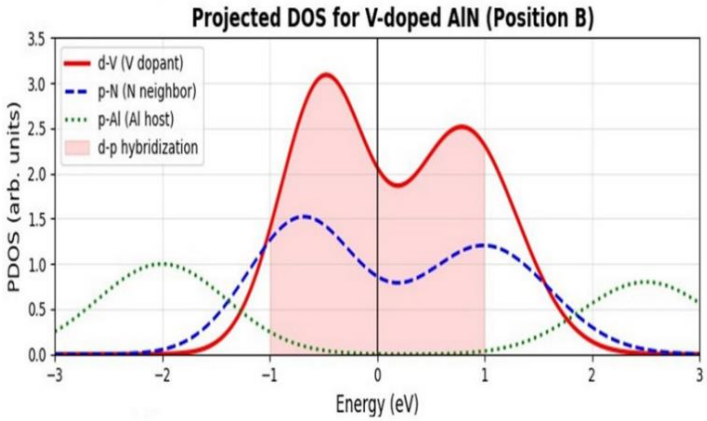


**Fig. 6.** Comparative analysis of surface charge density (σ) andtotale surface charge (S) for TM-doped AlN nanoribbons within the voltage window −0.6 to +0.6 V. The ratios $\sigma_{anodic}/\sigma_{cathodic}$ and $S_{anodic}/S_{cathodic}$ are used to classify electrode behavior as anode, cathode, or symmetric.

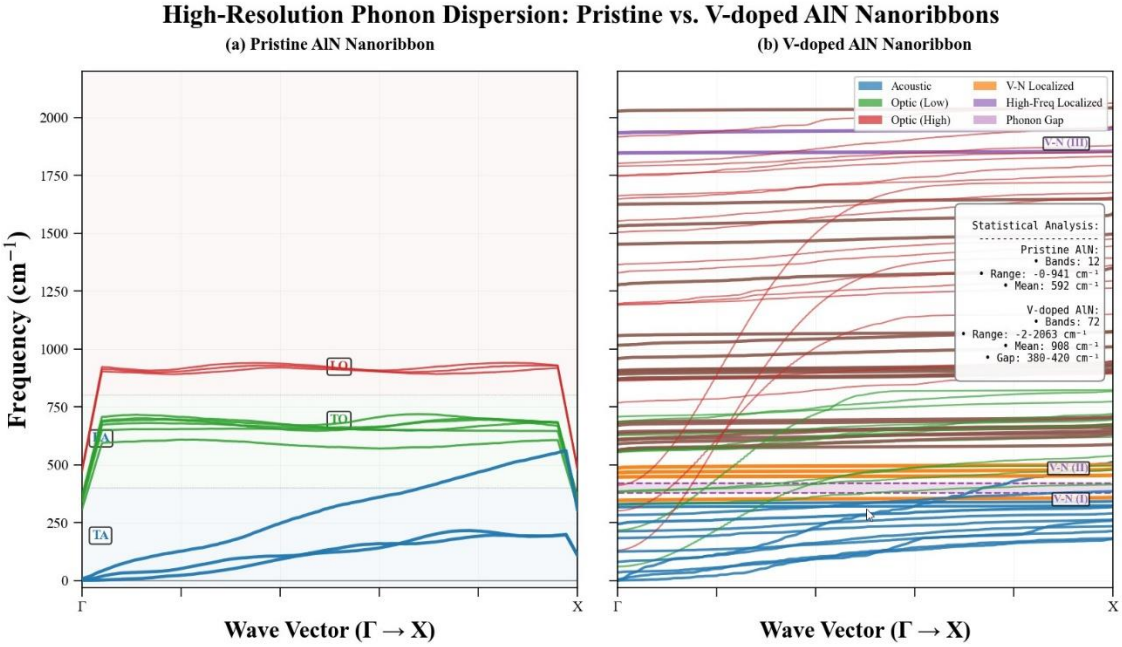


**Fig. 7.** (a) Phonon dispersion of a pristine AlN nanoribbon along the Γ–X direction, showing three acoustic and three optical branches. (b) Phonon dispersion of V-doped AlN nanoribbon, exhibiting additional flat, localized modes and phonon gaps resulting from dopant-induced symmetry breaking.

**Table 2.** Surface charge density (σ, mC/cm$^2$) and total surface charge (S, mC/cm$^2$·V) for transition metal-doped AlN nanoribbons at positions A, B, and C. This table summarizes the electrochemical performance of AlN nanoribbons doped with Sc, Ti, V, Mn, Fe, and Co atoms at three distinct structural positions.

| Material | Region | $\sigma_a$ | $\sigma_c$ | $S_a$ | $S_c$ |
|---|---|---|---|---|---|
| **Sc** | A | 0.009 | -0.002 | 4.735 | -8.295 |
| | B | 7.351 | -8.955 | 2.192 | -2.695 |
| | C | 0.001 | -0.001 | 4.122 | -1.744 |
| **Ti** | A | 8.220 | -5.838 | 1.299 | -1.148 |
| | B | 6.074 | -6.046 | 1.505 | -1.506 |
| | C | 8.018 | -5.392 | 0.984 | -0.838 |
| **V** | A | 29.188 | -32.113 | 9.011 | -9.382 |
| | B | 40.068 | -31.49 | 12.194 | -8.469 |
| | C | 12.679 | -19.135 | 2.59 | -2.802 |
| **Mn** | A | 0.526 | -3.176 | 0.028 | -0.214 |
| | B | 6.227 | -6.206 | 1.827 | -1.829 |
| | C | 5.324 | -12.208 | 0.805 | -1.52 |
| **Fe** | A | 6.503 | -6.064 | 1.578 | -1.554 |
| | B | 6.197 | -29.718 | 3.144 | -8.085 |
| | C | 13.317 | -24.367 | 4.779 | -6.194 |
| **Co** | A | 6.414 | -7.511 | 1.767 | -1.834 |
| | B | 0.454 | -1.406 | 0.019 | -0.084 |
| | C | 0.086 | -0.715 | 0.002 | -0.03 |

**Table 3.** Magnetic moments of transition metal-doped AlN nanoribbons. The calculated magnetic moments (in Bohr magnetons, μB) are listed for Sc, Ti, V, Mn, Fe, and Co dopants at the three substitutional sites (A: upper edge, B: center, C: lower edge). Dopants with partially filled d-orbitals (V, Mn, Fe) induce significant magnetic moments, crucial for spin-dependent electronic properties.

| Dopant | Position A | Position B | Position C |
|---|---|---|---|
| **Sc** | 0.00 | 0.00 | 0.00 |
| **Ti** | 0.05 | 0.07 | 0.06 |
| **V** | 1.12 | 1.08 | 1.10 |
| **Mn** | 1.95 | 1.92 | 1.94 |
| **Fe** | 2.10 | 2.05 | 2.08 |
| **Co** | 1.02 | 0.98 | 1.00 |

**Table 4.** Defect formation energies ($E_f$, in eV) for substitutional TM doping at Al sites in the AlN nanoribbon.

| Dopant | Position A | Position B | Position C |
|---|---|---|---|
| **Sc** | 1.2 | 1.2 | 0.8 |
| **Ti** | 0.9 | 0.9 | 0.7 |
| **V** | **0.5** | **0.6** | **0.4** |
| **Mn** | 1.0 | 1.1 | 0.9 |
| **Fe** | 1.3 | 1.4 | 1.2 |
| **Co** | 1.5 | 1.6 | 1.4 |

## 4. Conclusions

This study systematically demonstrates that transition metal doping is a highly effective strategy for tailoring the electronic properties and enhancing the energy storage performance of semiconducting AlN nanoribbons. Our density functional theory calculations reveal that the dopant type and its lattice position critically influence the electronic density of states, quantum capacitance, and surface charge density. Among the investigated dopants, vanadium emerges as the most effective, exhibiting the highest structural stability and a significant increase in quantum capacitance, thereby identifying V-doped nanoribbons as ideal candidates for anode applications. In contrast, cobalt-doped systems demonstrates superior cathodic surface charge density, making them suitable for cathode electrodes, while manganese offers a balanced charge storage profile for potential use in symmetric supercapacitors. The stability of all doped configurations was confirmed through phonon spectrum and cohesive energy calculations. Collectively, this work establishes a clear design principle for engineering semiconductor nanoribbons with customized electrochemical properties. Future research exploring solvation effects, the contribution of the double-layer capacitance, and experimental synthesis will be crucial for translating these theoretical insights into practical high-performance supercapacitor devices.

## Funding Statement

This research received no specific grant from any funding agency.

## Conflicts of interest

The authors declare that they have no known competing financial interests or personal relationships that could have appeared to influence the work reported in this paper.

## Authors contribution statement

Keyvan Moradian Koochaksaraei:
Conceptualization, Methodology, Software, Investigation, Writing – Original Draft.
Majid Vaezzadeh:
Supervision, Validation, Writing – Review & Editing.
All authors have read and agreed to the published version of the manuscript.

## References

[1] Kapse, S., Benny, B., Mandal, P. and Thapa, R., 2021. Design principle of $MoS_2$/C heterostructure to enhance the quantum capacitance for supercapacitor application. Journal of Energy Storage, 44, p.103476.
[2] Kolavada, H., Gajjar, P.N. and Gupta, S.K., 2024. Unraveling quantum capacitance in supercapacitors: Energy storage applications. Journal of Energy Storage, 81, p.110354.
[3] Zhou, Q., Wang, L., Ju, W., Su, D., Zhu, J., Yong, Y. and Wu, S., 2023. Quantum capacitance of graphene-like/graphene heterostructures for supercapacitor electrodes. *Electrochimica Acta*, *461*, p.142655.
[4] Sanglaow, T., Prasert, K., Chanthad, C., Liangruksa, M. and Sutthibutpong, T., 2024. A DFT study on the fundamental mechanisms of quantum capacitance enhancement within the carbon-based electrodes through different classes of doped configurations from biomass-derived elements. *Results in Materials*, *21*, p.100529.
[5] Guo, W., Yu, C., Li, S. and Qiu, J., 2021. Toward commercial-level mass-loading electrodes for supercapacitors: opportunities, challenges and perspectives. *Energy & Environmental Science*, *14*(2), pp.576-601.
[6] Horn, M., Gupta, B., MacLeod, J., Liu, J. and Motta, N., 2019. Graphene-based supercapacitor electrodes: Addressing challenges in mechanisms and materials. *Current Opinion in Green and Sustainable Chemistry*, *17*, pp.42-48.

[7] Zhou, Q., Ju, W., Yong, Y., Zhang, Q., Liu, Y. and Li, J., 2020. Effect of the N/P/S and transition-metal co-doping on the quantum capacitance of supercapacitor electrodes based on mono-and multilayer graphene. *Carbon*, *170*, pp.368-379.

[8] Hashemi, A., Naseri, M., Shahidi, M.M., Mojtabazadeh, H., Salehi, N. and Chireh, M., 2026. Synthesis and Investigation of Different Properties of $K_2FeO_4$/ZnO and Its GO-Based Nanocomposites. *Progress in Physics of Applied Materials*, *6*(1), pp.43-55.

[9] Haji, R. and Sanavi Khoshnood, D., 2026. Structural, Magnetic, and Electrical Properties of $REFe_{0.7}Cr_{0.3}O_3$ (RE= La, Pr, Nd, Sm, and Gd) Compounds. *Progress in Physics of Applied Materials*, *6*(1), pp.57-68.

[10] Kumar, A., Pant, M., Mishra, D., Kaur, G., Kumar, D., Kaur, R., Blamah, B.K., Kumar, N., Rustagi, S. and Singh, D., 2026. Sustainable Gold Nanoparticles Possessed Significant Activity Against Cancer Cell Lines (MCF-7, HeLa, and A549). *Progress in Physics of Applied Materials*, *6*(2), pp.137-149.

[11] Kliros, G.S., 2020. Strain effects on the quantum capacitance of graphene nanoribbon devices. *Applied Surface Science*, *502*, p.144292.

[12] Yang, G.M., Zhang, H.Z., Fan, X.F. and Zheng, W.T., 2015. Density functional theory calculations for the quantum capacitance performance of graphene-based electrode material. *The Journal of Physical Chemistry C*, *119*(12), pp.6464-6470.

[13] Bo, Z., Wen, W., Chen, Y., Guo, X., Yang, H., Yan, J., Cen, K. and Liu, Z., 2024. Effect of nitrogen and transition-metal co-doping on quantum capacitance enhancement of graphene as supercapacitor electrodes: A density functional theory study. *Colloids and Surfaces A: Physicochemical and Engineering Aspects*, *680*, p.132686.

[14] Li, X.H., Li, S.S., Cui, X.H., Zhang, R.Z. and Cui, H.L., 2021. First-principle study of electronic properties and quantum capacitance of lithium adsorption on pristine and vacancy-defected O-functionalized Ti2C MXene. *Applied Surface Science*, *563*, p.150264.

[15] Chandiramouli, R., 2015. Exploring electronic transport properties of AlN nanoribbon molecular device–a first-principles investigation. *Solid State Sciences*, *39*, pp.45-51.

[16] Giannozzi, P., Andreussi, O., Brumme, T., Bunau, O., Nardelli, M.B., Calandra, M., Car, R., Cavazzoni, C., Ceresoli, D., Cococcioni, M. and Colonna, N., 2017. Advanced capabilities for materials modelling with Quantum ESPRESSO. *Journal of physics: Condensed matter*, *29*(46), p.465901.

[17] Perdew, J.P., Burke, K. and Ernzerhof, M., 1996. Generalized gradient approximation made simple. *Physical review letters*, *77*(18), p.3865.

[18] Monkhorst, H.J. and Pack, J.D., 1976. Special points for Brillouin-zone integrations. *Physical review B*, *13*(12), p.5188.

[19] Zheng, F.L., Zhang, J.M., Zhang, Y. and Ji, V., 2010. First-principles study of the perfect and vacancy defect AlN nanoribbon. *Physica B: Condensed Matter*, *405*(17), pp.3775-3781.

[20] Du, A.J., Zhu, Z.H., Chen, Y., Lu, G.Q. and Smith, S.C., 2009. First principle studies of zigzag AlN nanoribbon. *Chemical physics letters*, *469*(1-3), pp.183-185.

[21] Zhang, C.W., 2012. First-principles study on electronic structures and magnetic properties of AlN nanosheets and nanoribbons. *Journal of Applied Physics*, *111*(4).

[22] Ghasemzadeh, F. and Kanjouri, F., 2019. Electronic and optical properties of AlN nanosheet under uni-axial strain. *International Journal of Nanoscience and Nanotechnology*, *15*(1), pp.21-26.

[23] Mousavi-Khoshdel, M., Targholi, E. and Momeni, M.J., 2015. First-principles calculation of quantum capacitance of codoped graphenes as supercapacitor electrodes. *The Journal of Physical Chemistry C*, *119*(47), pp.26290-26295.

[24] Reddy, A.S., Bhattacharya, S., Bhattacharjee, A. and Kanungo, S., 2024. EDL supercapacitor electrode performance analysis of group-VIB and group-X transition metal adsorbed and doped graphene: a density functional theory based comparative investigation. *ACS Applied Electronic Materials*, *6*(7), pp.5301-5313.

[25] Jalilian, J., Rezaei, G., Vaseghi, B., Zare, E., Taghizadeh, F. and Mardani-Fard, H.A., 2025. Quantum capacitance of decorated and doped B9 boron monolayer as electrodes for supercapacitors: Density Functional theory. *Journal of Energy Storage*, *107*, p.114843.